

1 Pre-print Statement for

2 **“Fe₅S₂ identified as a host for sulfur in Earth’s core”**

3 **Claire C. Zurkowski^{a,†}, Barbara Lavina^{b,c}, Abigail Case^a, Kellie Swadba^a, Stella Chariton^b,**
4 **Vitali B. Prakapenka^b, Andrew J. Campbell^a**

5
6 ^aThe University of Chicago, Department of the Geophysical Sciences, 5734 S Ellis Ave, Chicago, IL 60637, USA

7 ^bCenter for Advanced Radiation Sources, The University of Chicago, 9700 South Cass Avenue, Lemont, IL 60439,
8 USA

9 ^cX-ray Science Division, Advanced Photon Source, Argonne National Laboratory, Lemont, IL 60439, USA

10 [†]Now at Earth and Planets Laboratory, Carnegie Institution for Science, 5251 Broad Branch Road, NW,
11 Washington, DC 20015, USA

12
13
14 Corresponding Author: Claire Zurkowski, czurkowski@carnegiescience.edu

15
16 Dear Earth Arxiv,

17 This manuscript is a non-peer reviewed preprint submitted to *EarthArXiv*. It has been
18 submitted for peer review at *Nature Geoscience*.

19
20
21 Sincerely,

22 Claire Zurkowski

23
24
25
26
27
28
29
30
31
32
33
34

35 **Fe₅S₂ identified as a host for sulfur in Earth's core**

36 **Claire C. Zurkowski^a †, Barbara Lavina^{b,c}, Abigail Case^a, Kellie Swadba^a, Stella Chariton^b,**
37 **Vitali B. Prakapenka^b, Andrew J. Campbell^a**

38
39 ^aThe University of Chicago, Department of the Geophysical Sciences, 5734 S Ellis Ave, Chicago, IL 60637, USA

40 ^bCenter for Advanced Radiation Sources, The University of Chicago, 9700 South Cass Avenue, Lemont, IL 60439,
41 USA

42 ^cX-ray Science Division, Advanced Photon Source, Argonne National Laboratory, Lemont, IL 60439, USA

43 [†]Now at Earth and Planets Laboratory, Carnegie Institution for Science, 5251 Broad Branch Road, NW,
44 Washington, DC 20015, USA

45
46
47 Corresponding Author: Claire Zurkowski, czurkowski@carnegiescience.edu

48 **Abstract**

49
50 Planetary habitability, as we experience on Earth, is linked to a functioning geodynamo
51 which is in part driven by the crystallization of the liquid iron-nickel-alloy core as a planet cools
52 over time. Cosmochemical considerations suggest that sulfur is a candidate light alloying
53 element in rocky planetary cores of varying sizes and oxidation states; such that, iron sulfide
54 phase relations at extreme conditions contribute to outer core thermochemical convection and
55 inner core crystallization in a wide range of planetary bodies. Here we experimentally investigate
56 the structural properties of the Fe-S system and report the discovery of the sulfide, Fe₅S₂,
57 crystallizing in equilibrium with iron at Earth's outer core pressures and high temperatures.
58 Using single-crystal X-ray diffraction techniques, Fe₅S₂ was determined to adopt the complex
59 Ni₅As₂-type structure (*P*6₃*cm*, *Z* = 6). These results conclude that Fe₅S₂ is likely to crystallize at
60 the interface of Earth's core and mantle and will begin to crystallize during the freezing out of
61 Earth and Venus' core overtime. The increased metal-metal bonding measured in Fe₅S₂
62 compared to the other high *P-T* iron sulfides may contribute to signatures of higher conductivity
63 from regions of Fe₅S₂ is crystallization. Fe₅S₂ could serve as a host for Ni and Si as has been

64 observed in the related meteoritic phase, perryite, $(\text{Fe, Ni})_8(\text{P, Si})_3$, adding intricacies to
65 elemental partitioning during inner core crystallization. The stability of Fe_5S_2 presented here is
66 key to understanding the role of sulfur in the multicomponent crystallization sequences that drive
67 the geodynamics and dictate the structures of Earth and rocky planetary cores.

68

69 **Introduction**

70 Earth and the other terrestrial planets along with rocky exoplanets that continue to be
71 discovered are composed of silicate mantles and iron-rich metallic cores (e.g. Birch 1952; Scott
72 and Wasson 1975; Jephcoat and Olsen 1987; McDonough and Sun 1995; Rubie et al. 2011). The
73 likelihood of planetary habitability as we know it demands the presence of a geomagnetic field,
74 sustained by a convecting metallic liquid core, that protects the planet from harmful cosmic rays
75 (e.g. Buffet, 2000). In Earth's liquid outer core, the presence of light alloying elements
76 introduces complex pressure-temperature-dependent melting and crystallization thermodynamics
77 that drives core convection (Fearn and Loper, 1981; Stevenson 1981; 1988; Nimmo 2015).

78 While there remains no method to directly sample Earth's or any terrestrial planetary core, iron
79 meteorites are recognized as relics of the cores of planetesimal building blocks of terrestrial
80 planets, and have long provided insight into the cosmochemically abundant light elements
81 contributing to planetary core dynamics (e.g. Scott and Wasson 1975; Malvin et al. 1984). Of the
82 candidate core-alloying elements such as Si, O, S, C, and H, sulfur is present in nearly all iron
83 meteorites, suggesting that sulfur is a core alloying element in rocky planets with varying sizes,
84 oxidation states, and formation histories (Scott and Wasson 1975; Jones and Drake, 1983;
85 Kruijer et al. 2014). Examination of the structural properties of iron sulfides at high pressures

86 and temperatures (P - T) is therefore critical to ascertaining the chemistry and thermodynamics of
87 Earth, terrestrial and exoplanetary cores.

88 At present, the crystallographic assessment of iron sulfides at Earth and planetary core
89 conditions remains limited, even though properties such as density and elasticity are directly
90 related to the atomic arrangement of core-crystallizing phases and are critical for assessing the
91 seismic and dynamic observations of planetary cores. Previous work on Fe-rich systems indicate
92 that tetragonal Fe_3S (Fe_3P -type structure) is stable from Martian core conditions to Earth's outer
93 core conditions (Fei et al. 2000; Kamada et al. 2010; Ozawa et al. 2013; Mori et al. 2017), and an
94 orthorhombic Fe_2S (Co_2Si -type structure) phase becomes stable near Earth's inner-core boundary
95 (ICB) conditions (Tateno et al. 2019). The presence of Si has also been observed to stabilize the
96 $\text{Fe}_2(\text{S}, \text{Si})$ chemistry over Fe_3S at Mercurian core-mantle-boundary (CMB) conditions (Tao and
97 Fei 2021). These reports were predominantly based powder X-ray diffraction studies at high
98 pressures and temperatures and chemical analyses of recovered samples. However, recent work
99 has demonstrated that the iron-sulfur phase diagram is more complex at high P - T , but that this
100 complexity requires a superior method for accurately characterizing crystal structures at extreme
101 conditions. Using single-crystal X-ray diffraction techniques on multigrain samples, Co_2P -type
102 Fe_2S ($Pnma$, $Z = 4$) was recently identified and characterized at 90 GPa (Zurkowski et al. *in*
103 *press*). It remains, however, that these methods have not been applied to iron-sulfide phases
104 synthesized at high temperatures above 90 GPa, leaving the role of sulfur in the crystallization
105 sequences occurring in Venus, Earth and larger rocky exoplanets open to further discovery.

106

107

108 **Results and Discussion**

109 In the current study, Fe-rich Fe-S compositions were probed using both single-crystal and
110 powder X-ray diffraction techniques in a laser-heated diamond anvil cell to 200 GPa and 3300 K.
111 At high temperatures between 120 and 200 GPa, spanning Earth's CMB to mid-outer-core
112 conditions, crystallization of hcp-Fe (Figure 1a) is observed in the diffraction patterns along with
113 diffuse streaks and sets of closely spaced reciprocal nodes (Figure 1a, Figure S1), suggesting a
114 complex atomic arrangement of the coexisting sulfide. Upon temperature quenching in this
115 pressure range, diffraction images were collected while rotating the DAC across a +/- 17–30°
116 range (depending on the DAC configuration). Grains of a hexagonal lattice were identified in the
117 reciprocal space with indexed parameters: $a = 5.979(3) \text{ \AA}$, $11.088(6) \text{ \AA}$ at 140(2) GPa and
118 3070(180) K (Table S1). Assessment of the systematic absences for the structure factors reduced
119 for this hexagonal sulfide suggests a $P6_3cm$ space group, and structural solution and positional
120 and displacement parameter refinement converged to the Ni_5As_2 -type Fe_5S_2 ($Z=6$) (Table S2, S3;
121 Figure 2) (Oryshchyn et al. 2011). The Ni_5As_2 -type Fe_5S_2 is derived from the Pb_5Sb_2 structure
122 (El-Boragy et al. 1970) where the Fe6 site (Table S3) is split about its position and given half
123 occupancy, changing its Wyckoff site from $6c$ to $12d$ (Oryshchyn et al. 2011) (Figure 2, Table
124 S3, Appendix A1). Within error, all sites are fully occupied, except the Fe6 site that is ascribed
125 half occupancy (Oryshchyn et al. 2011).

126 Additionally, two polytypes associated with stacking variations along the c direction were
127 measured at lower temperatures and in stiff pressure media (Table S1). The Fe_5S_2 polytypism is
128 accompanied by observations of diffuse scattering between reciprocal nodes along the c direction
129 (Figure S1), indicating positional disorder as the atoms configure at high temperatures.
130 Analogous polytypes have been reported in related phases such as Pb_5Sb_2 (Saini et al. 1964).

131 X-ray diffraction from seven heating cycles performed between 100 and 200 GPa and to
132 3300 K provide insight into the Fe-rich Fe-S phase relations at outer core pressures and to high
133 temperatures. In each heating experiment, temperatures near melting were attained, and lattices
134 of Fe₅S₂ were indexed in the reciprocal space upon quenching. By further probing locations
135 across the thermal gradient of the laser heated spots, additional Fe-sulfides were characterized,
136 offering information on the lower temperature Fe-saturated sulfide crystal chemistries (Table S1,
137 S2). These include the Fe₃P-type Fe₃S (*I*-4, *Z* = 8) phase (Fei et al. 2000; Seagle et al. 2006;
138 Morard et al. 2007; Kamada et al. 2010; Kamada et al. 2012; Thompson et al. 2020), the *C*23
139 Fe₂S (Co₂P-type, *Pnma*, *Z* = 4) phase, and the *C*37 Fe₂S (Co₂Si-type, *Pnma*, *Z*=4) phase, in lower
140 temperature regions at 119 GPa, 131 GPa, and 140 GPa, respectively (Figure 3; Table S1, S2).
141 Notably, identification and crystal-structure analysis of Fe₅S₂ and Fe₃S in these Fe-saturated
142 experiments clarifies that Fe₅S₂, not Fe₃S is stable on the solidus above 120 GPa, despite reports
143 from previous powder diffraction studies (e.g. Kamada et al. 2010; Kamada et al. 2012; Ozawa
144 et al. 2013; Mori et al. 2017).

145 Comparison of the interatomic distances and coordination environments in the Fe-
146 sulfides observed in this study separates Fe₅S₂ as particularly unique among them. Within an
147 interatomic distance of 2.7 Å (Table S4, Appendix A1-A4), *C*23 and *C*37 Fe₂S consist of Fe sites
148 coordinated only by S, Fe₃S marks an increase in Fe-Fe bonding with Fe surrounded by up to 9
149 Fe sites, and Fe₅S₂ exhibits Fe surrounded by up to 9 Fe sites with Fe-Fe bond lengths up to 25%
150 shorter in Fe₅S₂ compared to Fe₃S (Table S4). Following previous descriptions of related *M*₅*X*₂
151 phases (e.g. (Kjekshus et al. 1973; Oryshchyn et al. 2011), Fe₅S₂ can be viewed as an
152 arrangement of 6 Fe sites and 3 S sites with the Fe1, Fe2, Fe4, and Fe6 sites in 13-fold

153 coordination, the Fe3 and Fe5 sites in 12-fold coordination, and the S sites in 10-fold
154 coordination (Figure 2c, Table S4). All sites are coordinated by both Fe and S sites.

155 The presented single-crystal derived structures of Fe₅S₂, Fe₃S, C23 Fe₂S, and C37 Fe₂S
156 were then used to interpret the changes in powder X-ray diffraction patterns collected during
157 heating between 110 and 200 GPa and to ~3300 K (Figure 4, Figure S4). C23 Fe₂S is observed
158 coexisting with Fe to ~125 GPa and up to ~2300 K. In combination with previous studies, C23
159 Fe₂S is stable at moderate temperatures between 25 and 125 GPa (Zurkowski et al. *in press*,
160 Zurkowski et al. submitted). A pressure-induced C23–C37 Fe₂S transition is constrained between
161 125 and 135 GPa, in agreement with previous investigations of Fe₂S (Zurkowski et al.
162 submitted). C37 Fe₂S is stable between 130–200 GPa and to ~3000 K in this study, and previous
163 work suggests that C37 Fe₂S may remain stable to 306 GPa at high temperatures (Tateno et al.
164 2019). Tetragonal Fe₃S forms from the reaction of C23 Fe₂S + Fe between 2000–2400 K at ~115
165 GPa. The stability of tetragonal Fe₃S is constrained to pressures below ~120 GPa at high
166 temperatures in Fe-rich systems (Figure 4) (Seagle et al. 2006; Morard et al. 2008; Kamada et al.
167 2010; Kamada et al. 2012; Thompson et al, 2020). Fe₅S₂ is observed coexisting with iron
168 between ~120–200 GPa and in the 2400–3300 K range, making it the relevant sulfide in the
169 melting and crystallization properties of Fe-rich metallic cores at these pressures (Figure 4).

170 **Sulfur in Earth and planetary cores**

171 The stability of Fe₅S₂ and the phase relations observed in this study present novel
172 constraints on the material properties of Fe-sulfides at conditions relevant to Earth's outer core,
173 Venus' core, and exoplanetary cores of similar size and core-mass fraction (CMF). Namely, at
174 pressures ≥ 120 GPa, Ni₅As₂-type Fe₅S₂, not tetragonal Fe₃S as previously believed, is the

175 relevant Fe-rich sulfide. As Earth's outer core crystallizes over time, Fe_5S_2 will eventually
176 crystallize over a large depth range up to the CMB. Tetragonal Fe_3S has been confirmed up to
177 120 GPa (Figure 4) (Seagle et al. 2006; Morard et al. 2008; Thompson et al., 2020), constraining
178 the $\text{Fe}_3\text{S} + \text{Fe} \rightarrow \text{Fe}_5\text{S}_2 + \text{Fe}$ transition to ~ 120 GPa. Rocky planetary bodies with sizes and CMFs
179 like that of Venus (CMB = 114 GPa) (Aitta 2012) would likely crystallize Fe_3S at the CMB,
180 while Fe_5S_2 will be crystallizing over much of the core's depth. $C37$ Fe_2S is reported to be stable
181 on the solidus above 306 GPa in Fe-rich systems (Tateno et al. 2019), suggesting a $\text{Fe}_5\text{S}_2 + \text{Fe} \rightarrow$
182 $\text{Fe}_2\text{S} + \text{Fe}$ transition in the 200–300 GPa range. $C37$ Fe_2S remains the candidate Fe-rich sulfide
183 at Earth's ICB, but for planets like Venus with a central pressure of 274 GPa (Aitta 2012), Fe_5S_2
184 may instead be the relevant Fe-rich sulfide, necessitating experimental determination of the
185 $\text{Fe}_5\text{S}_2 \rightarrow \text{Fe}_2\text{S} + \text{Fe}$ decomposition P - T boundary. Additional assessment of the volume and
186 melting-temperature changes across these newly determined sulfide transitions are critical for
187 matching the density and seismic profiles of Earth and rocky planetary cores. Furthermore, as
188 Fe_5S_2 exhibits a complex crystalline arrangement with significant metal-metal bonding compared
189 to Fe_2S and Fe_3S at core pressures, the significant depth over which Fe_5S_2 crystallizes in and
190 Venus- to Earth-sized planetary cores is likely to contribute to higher conductivity signatures in
191 these regions.

192 Terrestrial core chemistries are multicomponent; Si and Ni are also important core-
193 alloying elements in planets such as Earth, drawing attention to the potential stability of the
194 perryite $(\text{Fe}, \text{Ni})_8(\text{Si}, \text{P})_3$ structure in $(\text{Fe}, \text{Ni}) - (\text{Si}, \text{S})$ -rich cores. Perryite, is a mineral observed
195 in enstatite chondrites and aubrites that adopts a structure that is trigonal stacking variant of the
196 Ni_5As_2 -type structure (Wasson and Wai, 1970; Okada et al. 1991) and iron phosphides tend to
197 adopt analogous structures to that observed in iron sulfides (i.e., Fei et al. 2000; Dera et al. 2008;

198 Gu et al. 2014; Gu et al. 2016; Zurkowski et al., in press). Fe_5S_2 could potentially serve as a host
199 for nickel and silicon in the perryite structure at Earth's outer core conditions. Further, Si has
200 recently been shown to dissolve into iron-sulfide phases and expand their stability fields with
201 pressure (Tao and Fei, 2021). The dissolution of silicon into Fe_5S_2 may expand its stability to
202 higher pressures, making it potentially relevant at Earth's ICB conditions. If this is the case, the
203 partitioning of Si and Ni between $(\text{Fe}, \text{Ni})_5(\text{S}, \text{Si})_2$ and $(\text{Fe}, \text{Ni}, \text{Si})$ and the density difference
204 between the inner-core-crystallizing phase and remaining light-element-rich liquid will be crucial
205 to investigations of the inner-core-density deficit and inner core seismic morphology.

206

207 **Materials and Methods**

208 Experiments targeting multigrain synthesis in the Fe-S system consisted of mixtures of Fe
209 (99.9+%, $<10\mu\text{m}$, Alfa Aesar) and iron sulfide (FeS , 99.99%, Alfa Aesar) in Fe+12.5 wt% S
210 ($\text{Fe}_{80}\text{S}_{20}$), Fe + 23 wt% S ($\text{Fe}_{67}\text{S}_{33}$) compositions. The Fe-FeS compositions were ground in
211 ethanol in a pestle and mortar for 1 hour then mixed dry for a short interval to homogenize any
212 density settling during alcohol evaporation.

213 Pressure was generated using BX-90-type (Kantor et al. 2012) diamond anvil cells (DAC)
214 with type 1 Boehler-Almax conical diamonds and seats, and Mao symmetric-type DACs with
215 Type 1 standard cut diamonds mounted on tungsten carbide or cubic-boron nitride (cBN) seats.
216 Diamond culets ranged from 150-50 μm in diameter. Foils of $\text{Fe}_{80}\text{S}_{20}$ or $\text{Fe}_{67}\text{S}_{33}$ were produced
217 by pressing the Fe-S starting powders between two ungasketed diamond anvils, then loaded
218 between pellets of KCl or SiO_2 . Sample chambers ranged from 180-25 μm in diameter and were
219 drilled from pre-indented rhenium gaskets. Samples were dried at 100°C for 30 minutes prior to
220 pressurization.

221 Angle dispersive X-ray diffraction (XRD) experiments were conducted at Argonne
222 National Laboratory, sector 13 ID-D, of the Advanced Photon Source. At Sector 13 ID-D, a 2.5
223 $\mu\text{m} \times 3.54 \mu\text{m}$ full width, half maximum (FWHM) monochromatic X-ray beam tuned to 37 or 42
224 keV was utilized, and diffracted X-rays were collected with a CdTe 1M Pilatus detector. Sample-
225 to-detector geometries were calibrated using a LaB₆ NIST standard and a single crystal of
226 enstatite was used for calibration of the rotational geometry of the X-ray beam and detector.

227 Double-sided laser heating and *in-situ* XRD collection took place at Sector 13 ID-D. Fibers
228 lasers shaped with $\sim 10 \mu\text{m}$ radius flat tops were aligned with the X-ray beam using the X-ray
229 fluorescence of the sample pressure media or the gasket (Prakapenka et al., 2008). During
230 heating, thermal emission from a $6 \mu\text{m}$ central region of the laser-heated spot was measured
231 spectroradiometrically and fit to a gray body approximation (Heinz and Jeanloz, 1987). A 3%
232 temperature correction was then applied to correct for axial gradients through the sample
233 (Campbell et al., 2007; 2009). The laser power on each side of the sample was adjusted to
234 maintain uniform double-sided heating and X-Ray diffraction and temperature measurements
235 were collected every $\sim 200 \text{ K}$ with 1s exposure times. Samples were typically quenched at high
236 temperatures within 30-45 minutes of heating or after a phase transition and suitable grain
237 growth was observed. Powder diffraction patterns were processed using Dioptas (Prescher and
238 Prakapenka, 2015) and CrysAlisPro (Rigaku OD, 2018). Pressure was determined using the
239 equation of state of hcp-Fe (Dewaele et al. 2006).

240 Upon quenching, X-ray diffraction maps of the heated spot were collected across a 100
241 μm^2 square region in $3 \mu\text{m}$ steps. Map locations showing high intensity, spotty diffraction
242 patterns were chosen for multigrain single-crystal type X-ray diffraction collection approach, as
243 these features indicate high-temperature induced crystallite growth. At chosen map locations, X-

244 ray diffraction images were collected across ± 17 to $\pm 30^\circ$ rotational scans in 0.25° – 0.5° steps with
245 1–4 s exposure times. The diffraction reflections were then mapped in the reciprocal space and
246 target grains were identified and separated from reflections associated with the pressure media,
247 iron, and diamond (Rigaku OD, 2018).

248 Target Fe-S lattices were then indexed and the peak intensities were integrated and reduced
249 using CrysalisPro (Rigaku OD, 2018). Absorption corrections and scaling factors were applied to
250 the structure factors in CrysalisPro using the multi-scan method via the Scale3 Abspack program
251 (Rigaku OD, 2018). The final structure factors and lattice geometries were then refined to known
252 structure models (El-Boragy et al. 1970; Oryshchyn et al. 2011) using SHELXL2014/7
253 (Sheldrick 2015). Reflections showing anomalous calculated versus measured structure factors;
254 likely due to overlap with diamond and other phases in the multigrain sample, resolution
255 limitations, and volume of crystal illuminated by the X-ray beam, were omitted. Structure
256 models were visualized using Vesta during the refinement procedure (Momma and Izumi 2011).

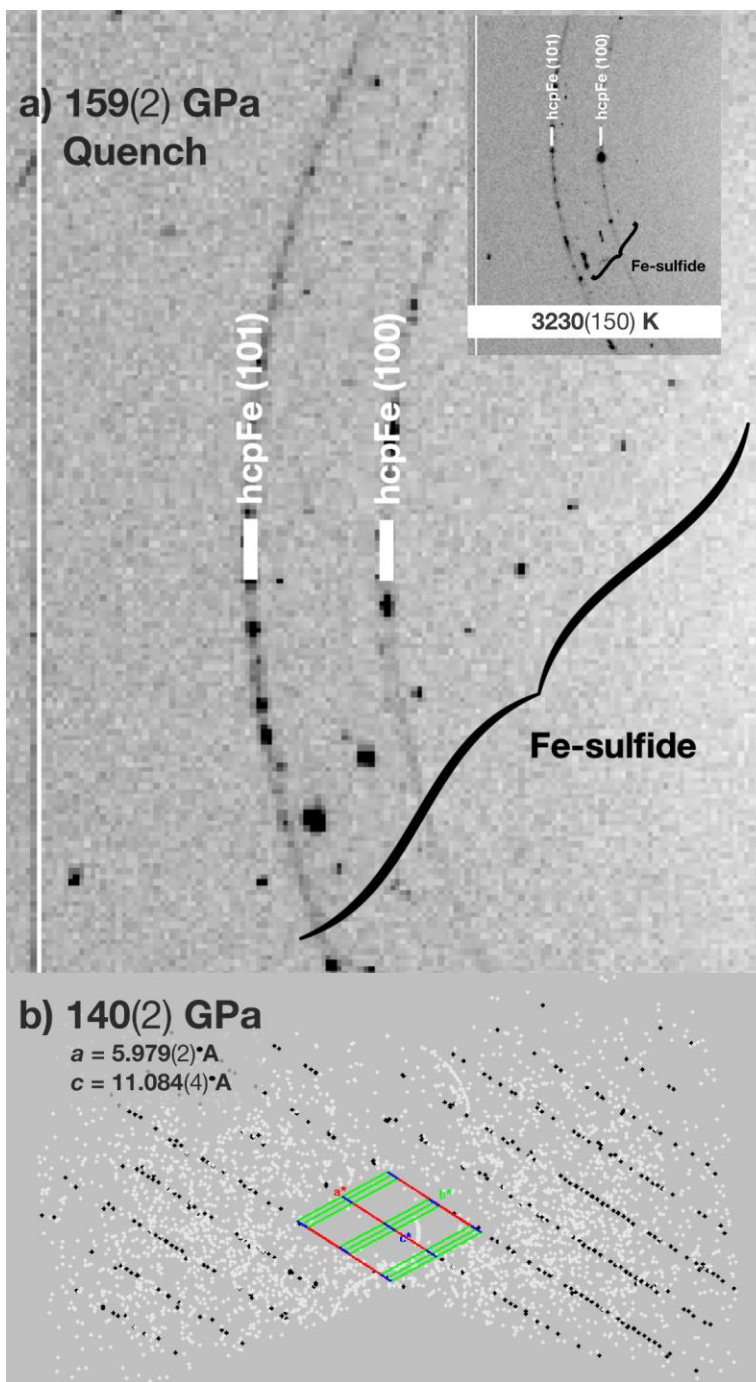
257

258 **Acknowledgments**

259 Portions of this work were performed at GeoSoilEnviroCARS (The University of Chicago,
260 Sector 13), Advanced Photon Source (APS), Argonne National Laboratory.
261 GeoSoilEnviroCARS is supported by the National Science Foundation - Earth Sciences (EAR -
262 1634415). This research used resources of the Advanced Photon Source, a U.S. Department of
263 Energy (DOE) Office of Science User Facility operated for the DOE Office of Science by
264 Argonne National Laboratory under Contract No. DE-AC02-06CH11357. Use of the
265 COMPRES-GSECARS gas loading system was supported by COMPRES under NSF
266 Cooperative Agreement EAR -1606856 and by GSECARS through NSF grant EAR-1634415

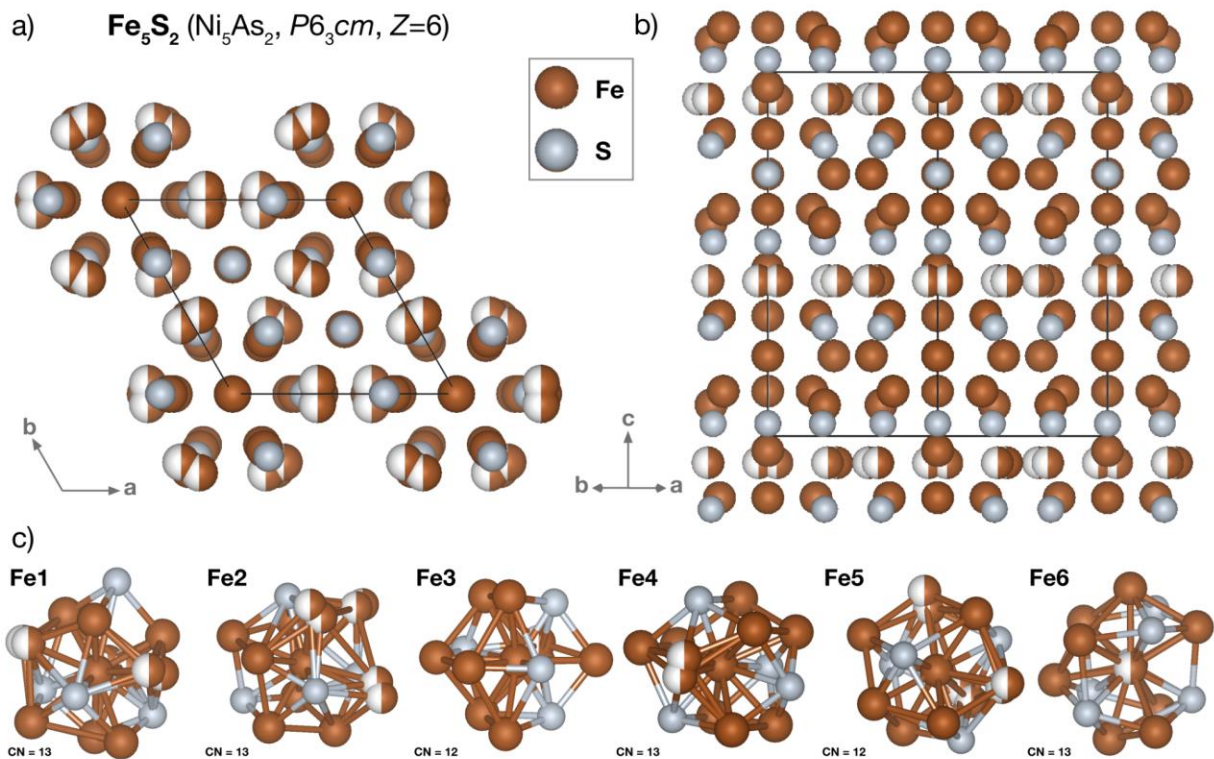
267 and DOE grant DE-FG02-94ER14466. This research used resources of the Advanced Photon
268 Source, a U.S. Department of Energy (DOE) Office of Science User Facility operated for the
269 DOE Office of Science by Argonne National Laboratory under Contract No. DE-AC02-
270 06CH11357. This material is based upon work supported by a National Science Foundation
271 Graduate Research Fellowship to C.C.Z. This work was also supported by the National Science
272 Foundation by grant EAR-1651017 to A.J.C.

273



275
276 **Figure 1. Fe₅S₂ diffraction in equilibrium with iron**

277 a) View of a crystallite of the high-temperature Fe₅S₂ coexisting with recrystallized hcp-Fe after
 278 synthesis at 159(2) GPa and 3230(130) K (inset). The spotty rings corresponding to the hcp-Fe
 279 (100) and (101) planes demonstrate that iron equilibrated at 159(2) GPa and 3230(130) K. b)
 280 View of the reciprocal space for reflections detected in an experiment on the Fe₈₀S₂₀ composition
 281 quenched from 140(2) GPa and 3070(140) K. The reciprocal lattice, colored in black, is
 282 associated with a Fe₅S₂ grain whose lattice parameters are provided in the top left.



283

284

Figure 2. Crystal structure of Ni_5As_2 -type Fe_5S_2

285

Crystal structure of Fe_5S_2 viewed along the a) c axis and the b) (100) plane. c) The Fe-

286

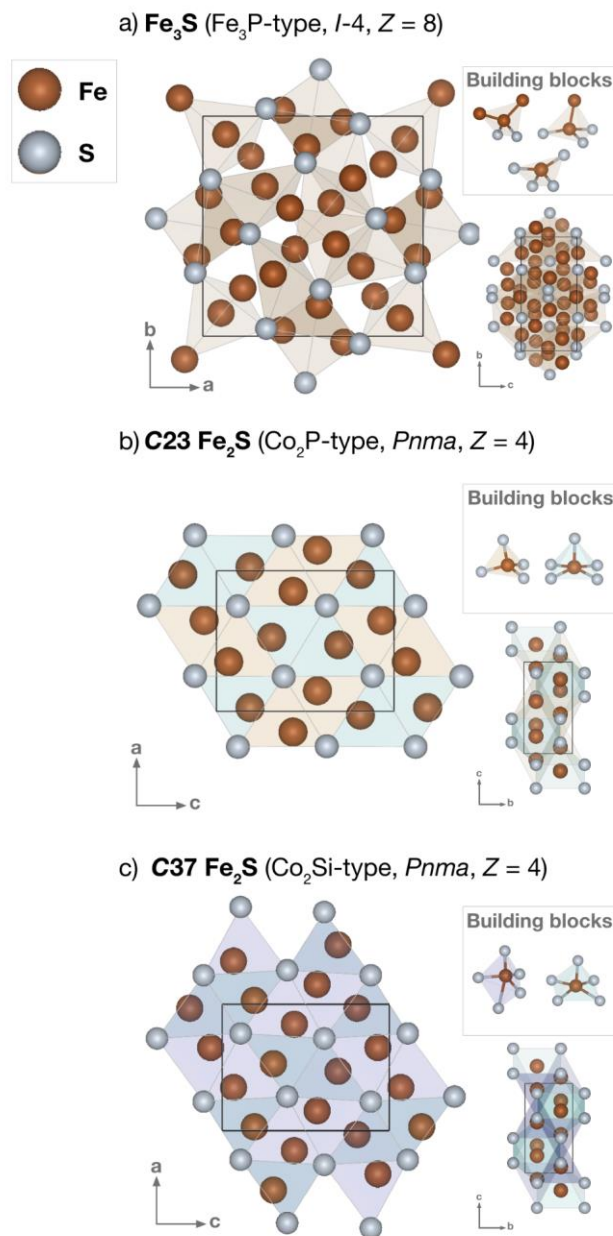
coordination polyhedra observed in this atomic arrangement are provided. Fe1, Fe2, Fe4, and

287

Fe6 are coordinated by 13 sites and Fe3 and Fe5 are coordinated by 12 sites. Each coordination

288

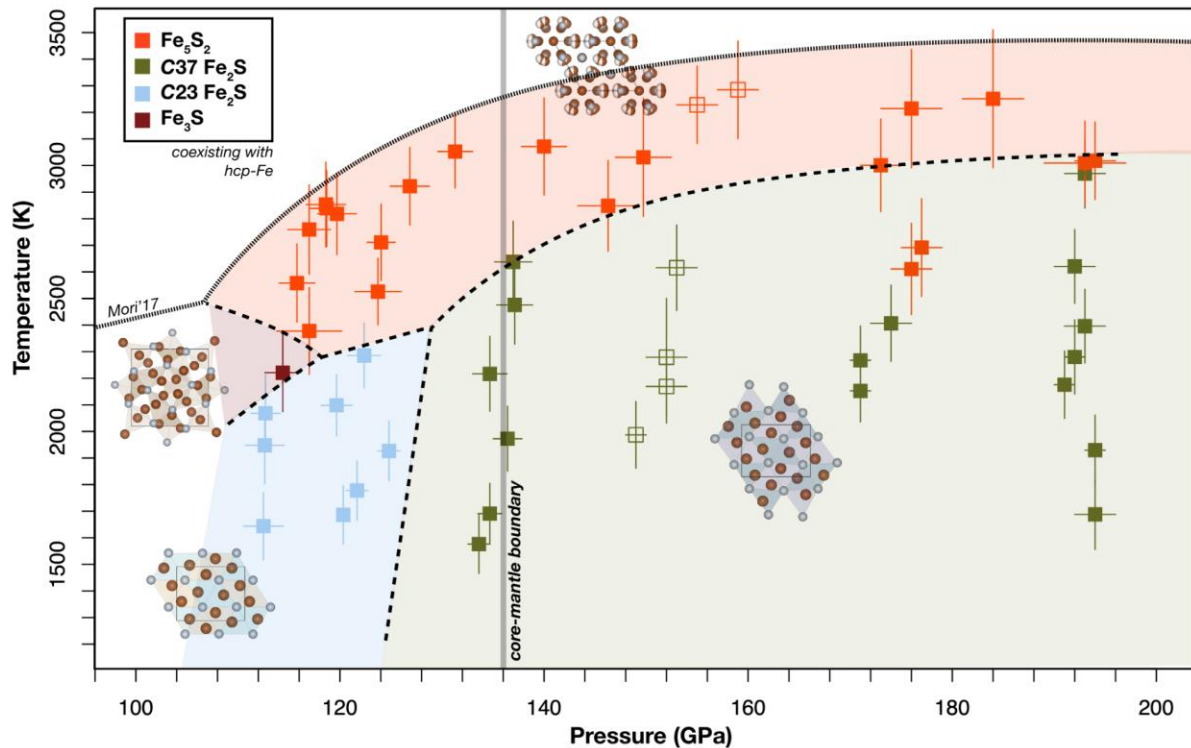
polyhedron consists of Fe and S sites.



289

290 **Figure 3. Crystal structures of Fe_3S and Fe_2S observed in this study**

291 a) Fe_3S adopts the Fe_3P -type structure ($I-4$, $Z = 8$) that is composed of three tetrahedrally
 292 coordinated Fe-sites, each with increasing Fe–Fe bonding. b) The $\text{C}23 \text{Fe}_2\text{S}$ structure (Co_2P -type,
 293 $Pnma$, $Z = 4$) is made up of columns of FeS_4 tetrahedra and columns of FeS_5 square pyramids
 294 linked along edges in the b direction. c) The $\text{C}37 \text{Fe}_2\text{S}$ structure (Co_2Si -type, $Pnma$, $Z = 4$) has
 295 the same site symmetries as the $\text{C}23$ structure, but is marked by a shortened a axis and elongated
 296 b and c axes accompanied by the formation of a 5-fold dipyramid.



297

298 **Figure 4. Iron-rich sulfide phase diagram to Earth's outer core pressures**

299 At moderate temperatures up to 130 GPa, C23 Fe₂S is observed. At moderate temperatures,
 300 tetragonal Fe₃S (Fe₃P-type) is observed below 120 GPa. At moderate temperatures between 130
 301 and 200 GPa, C37 Fe₂S is observed, and on the liquidus between ~115–200 GPa, Fe₅S₂ is the
 302 liquidus phase. A kink the Fe-S solidus curve (Mori et al. 2017), is presented to account for the
 303 change in phase relations and the high temperatures at which Fe₅S₂ was observed. The closed
 304 squares represent experiments conducted on the Fe₈₀S₂₀ starting material, and the open squares
 305 represent experiments conducted on the Fe₆₇S₃₃ starting material. Both show compatible results,
 306 likely indicating that Fe-rich regions of the Fe₆₇S₃₃ foils were probed.

307

308

309

310

311

312

313

314

315

316 **References**

- 317 Anzellini, S., Dewaele, A., Mezouar, M., Loubeyre, P. and Morard, G. (2013). Melting of iron at
318 Earth's inner core boundary based on fast X-ray diffraction. *Science*, 340, 464–466.
- 319 Birch, F. (1952) Elasticity and constitution of the Earth's interior. *Journal of Geophysical*
320 *Research*, 57, 227–286.
- 321 Buffett, B.A. (2000) Earth's core and the geodynamo. *Science*, 288, pp.2007-2012.
- 322 Campbell, A.J., Seagle, C.T., Heinz, D. L., Shen, G., and Prakapenka, V.B. (2007) Partial
323 melting in the iron-sulfur system at high pressure: A synchrotron X-ray diffraction study.
324 *Physics of the Earth and Planetary Interiors*, 162, 119–128.
- 325 Campbell, A.J., Danielson, L., Righter, K., Seagle, C.T., Wang, Y. and Prakapenka, V.B. (2009)
326 High pressure effects on the iron–iron oxide and nickel–nickel oxide oxygen fugacity
327 buffers. *Earth and Planetary Science Letters*, 286, 556–564.
- 328 Chen, J.H. and Whitmire, K.H. (2018) A structural survey of the binary transition metal
329 phosphides and arsenides of the d-block elements. *Coordination Chemistry Reviews*, 355,
330 271–327.
- 331 Dewaele, A., Loubeyre, P., Occelli, F., Mezouar, M., Dorogokupets, P.I. and Torrent, M. (2006)
332 Quasihydrostatic equation of state of iron above 2 Mbar. *Physical Review Letters*, 97,
333 215504.
- 334 Dziewonski, A.M. and Anderson, D.L. (1981) Preliminary reference Earth model. *Physics of the*
335 *Earth and planetary interiors*, 25, 297–356.
- 336 El-Boragy, M., Bhan, S. and Schubert, K. (1970) Kristallstruktur von Pd₅Sb₂ und Ni₅As₂ und
337 einigen varianten. *Journal of the Less Common Metals*, 22, 445–458.
- 338 Evans, H.T. (1970) Lunar troilite: crystallography. *Science*, 167, 621–623.
- 339 Fearn, D.R. and Loper, D.E., (1981). Compositional convection and stratification of Earth's core.
340 *Nature*, 289, 393–394.
- 341 Fei, Y., Prewitt, C.T., Mao, H.K. and Bertka, C.M (1995). Structure and density of FeS at high
342 pressure and high temperature and the internal structure of Mars. *Science*, 268, 1892–
343 1894.
- 344 Fei, Y., Bertka, C.M. and Finger, L.W. (1997) High-pressure iron-sulfur compound, Fe₃S₂, and
345 melting relations in the Fe–FeS system. *Science*, 275, 1621–1623.
- 346 Fei, Y., Li, J., Bertka, C.M. and Prewitt, C.T. (2000) Structure type and bulk modulus of Fe₃S, a
347 new iron-sulfur compound. *American Mineralogist*, 85, 1830–1833.
- 348 Fei, Y., Ricolleau, A., Frank, M., Mibe, K., Shen, G. and Prakapenka, V. (2007) Toward an
349 internally consistent pressure scale. *Proceedings of the National Academy of Sciences*,
350 104, 9182–9186.
- 351 Frank, K. and Schubert, K. (1971) Kristallstruktur von Ni₃₁Si₁₂. *Acta Crystallographica Section*
352 *B: Structural Crystallography and Crystal Chemistry*, 27, 916–920.
- 353 Heinz, D.L., and Jeanloz, R. (1987) Measurement of the melting curve of Mg_{0.9}Fe_{0.1}SiO₃ at
354 lower mantle conditions and its geophysical implications. *Journal of Geophysical*
355 *Research*, 92, 437–444.

356 Irving, J.C., Cottaar, S. and Lekić, V. (2018) Seismically determined elastic parameters for
357 Earth's outer core. *Science advances*, 4, 2538.

358 Jephcoat, A. and Olson, P., (1987) Is the inner core of the Earth pure iron? *Nature*, 325, 332–
359 335.

360 Jones, J.H. and Drake, M.J. (1983). Experimental investigations of trace element fractionation in
361 iron meteorites, II: The influence of sulfur. *Geochimica et Cosmochimica Acta*, 47,
362 1199–1209.

363 Kamada, S., Terasaki, H., Ohtani, E., Sakai, T., Kikegawa, T., Ohishi, Y., Hirao, N., Sata, N. and
364 Kondo, T. (2010) Phase relationships of the Fe–FeS system in conditions up to the
365 Earth's outer core. *Earth and Planetary Science Letters*, 294, 94–100.

366 Kamada, S., Ohtani, E., Terasaki, H., Sakai, T., Miyahara, M., Ohishi, Y. and Hirao, N. (2012)
367 Melting relationships in the Fe–Fe₃S system up to the outer core conditions. *Earth and*
368 *Planetary Science Letters*, 359, 26–33.

369 Kantor, I., Prakapenka, V., Kantor, A., Dera, P., Kurnosov, A., Sinogeikin, S., Dubrovinskaia, N.
370 and Dubrovinsky, L. (2012) BX90: A new diamond anvil cell design for X-ray
371 diffraction and optical measurements. *Review of Scientific Instruments*, 83, 125102.

372 King, H. and Prewitt, C.T. (1982) High-pressure and high-temperature polymorphism of iron
373 sulfide (FeS). *Acta Crystallographica Section B: Structural Crystallography and Crystal*
374 *Chemistry*, 38, 1877–1887.

375 Kjekshus, A., Skaug, K.E., Hebrew, C., Van Buren, C.T., Klæboe, P. and Swahn, C.G. (1973).
376 On the crystal structure of Ni₅As₂. *Acta Chem. Scand.*, 27, 582–588.

377 Kruijer, T.S., Touboul, M., Fischer-Gödde, M., Bermingham, K.R., Walker, R.J. and Kleine, T.,
378 2014a. Protracted core formation and rapid accretion of protoplanets. *Science*, 344,
379 1150–1154.

380 Kuwayama, Y., Morard, G., Nakajima, Y., Hirose, K., Baron, A.Q., Kawaguchi, S.I., Tsuchiya,
381 T., Ishikawa, D., Hirao, N. and Ohishi, Y. (2020). Equation of state of liquid iron under
382 extreme conditions. *Physical review letters*, 124, .165701.

383 Litasov, K.D., Shatskiy, A.F., Minin, D.A., Kuper, K.E. and Ohfuji, H. (2019). The Ni–Ni₂P
384 phase diagram at 6 GPa with implication to meteorites and super-reduced terrestrial
385 rocks. *High Pressure Research*, 39, 561–578.

386 Maaref, S., Madar, R., Chaudouet, P., Fruchart, R., Senateur, J.P., Averbuch-Pouchot, M.T.,
387 Bacmann, M., Durif, A. and Wolfers, P. (1983) Etude de la structure et des conditions de
388 stabilite d'un nouvel arseniure de fer: Fe₁₂As₅. *Materials Research Bulletin*, 18, 473-480.

389 Malvin, D.J., Wang, D. and Wasson, J.T. (1984) Chemical classification of iron meteorites—X.
390 Multielement studies of 43 irons, resolution of group IIIE from IIIAB, and evaluation of
391 Cu as a taxonomic parameter. *Geochimica et Cosmochimica Acta*, 48, 785–804.

392 Masters, G. and Gubbins, D. (2003) On the resolution of density within the Earth. *Physics of the*
393 *Earth and Planetary Interiors*, 140, 159–167.

394 McDonough, W.F. and Sun, S.S. (1995) The composition of the Earth. *Chemical geology*, 120,
395 223–253.

396 McDonough, W.F., (2003) 2.15–Compositional model for the earth’s core. *Treatise on*
397 *Geochemistry*, 547–568.

398 Momma, K. and Izumi, F. (2011) VESTA 3 for three-dimensional visualization of crystal,
399 volumetric and morphology data. *Journal of applied crystallography*, 44, 1272–1276.

400 Morard, G., Andrault, D., Guignot, N., Sanloup, C., Mezouar, M., Petitgirard, S. and Fiquet, G.
401 (2008). In situ determination of Fe–Fe₃S phase diagram and liquid structural properties
402 up to 65 GPa. *Earth and Planetary Science Letters*, 620–626.

403 Mori, Y., Ozawa, H., Hirose, K., Sinmyo, R., Tateno, S., Morard, G. and Ohishi, Y. (2017)
404 Melting experiments on Fe–Fe₃S system to 254 GPa. *Earth and Planetary Science Letters*,
405 464 135–141.

406 Murthy, V.R. and Hall, H.T. (1970) The chemical composition of the earth's core: Possibility of
407 sulfur in the core. *Physics of the Earth and Planetary Interiors*, 2, 276–282.

408 Nimmo, F. (2015) Thermal and compositional evolution of the core. In *Core Dynamics* (Ed.
409 Peter Olsen). Vol. 8 *Treatise on Geophysics*, (Exec. Eds. G. Schubert), 217–241.

410 Okada, A., Kobayashi, K., Ito, T. and Sakurai, T. (1991) Structure of synthetic perryite,
411 (Ni, Fe)₈(Si, P)₃. *Acta Crystallographica Section C: Crystal Structure Communications*,
412 47, 1358–1361.

413 Oryshchyn, S., Babizhetskyy, V., Zhak, O., Stoyko, S., Guérin, R., and Simon, A. (2011) Crystal
414 structure of HT-Ni₅P₂ and reinvestigation of isotypic Ni₅As₂. *Intermetallics*, 19,
415 1041–1046.

416 Ozawa, H., Hirose, K., Suzuki, T., Ohishi, Y. and Hirao, N. (2013) Decomposition of Fe₃S
417 above 250 GPa. *Geophysical research letters*, 40, 4845–4849.

418 Prakapenka, V.B., Kubo, A., Kuznetsov, A.Laskin, A., Shkurikhin, O., Dera, P., Rivers, M. L.
419 and Sutton, S.R. (2008) Advanced flat top laser heating system for high pressure research
420 at GSECARS: application to the melting behavior of germanium. *High Pressure*
421 *Research*, 28, 225–235.

422 Prescher, C., and Prakapenka, V.B. (2015) DIOPTAS: a program for reduction of two
423 dimensional X-ray diffraction and data exploration. *High Pressure Research*, 35(3), 223–
424 230.

425 Ricard, Y., Šrámek, O. and Dubuffet, F. (2009) A multi-phase model of runaway core–mantle
426 segregation in planetary embryos. *Earth and Planetary Science Letters*, 284, 144–150.

427 Rigaku Oxford Diffraction (2018) CrysAlisPRO software system, ver. 1.171.39.44a Rigaku
428 Corporation, Oxford, U.K.

429 Ringwood, A.E. (1966) The chemical composition and origin of the Earth. *Advances in earth*
430 *science*, 65, 287.

431 Rubie, D.C., Frost, D.J., Mann, U., Asahara, Y., Nimmo, F., Tsuno, K., Kegler, P., Holzheid, A.
432 and Palme, H. (2011) Heterogeneous accretion, composition and core–mantle
433 differentiation of the Earth. *Earth and Planetary Science Letters*, 301, 31–42.

434 Rundqvist, S. (1960) The structures of Co₂P, Ru₂P and related phases. *Acta Chemica*
435 *Scandinavica*, 14, 1961–1979.

436 Rundqvist, S. and Jellinek, F. (1959) The structures of Ni₆Si₂B, Fe₂P and some related phases.
437 Acta Chemica Scandinavica, 13, 425–432.

438 Saini, G.S., Calvert, L.D., and Taylor, J.B. (1964). Compounds of the type M₅X₂: Pd₅As₂, Ni₅Si₂,
439 and Ni₅P₂. Canadian Journal of Chemistry, 42, 1511–1517.

440 Scott, E.R. and Wasson, J.T. (1975) Classification and properties of iron meteorites. Reviews of
441 Geophysics, 13, 527–546.

442 Seagle, C.T., Campbell, A.J., Heinz, D.L., Shen, G. and Prakapenka, V.B. (2006) Thermal
443 equation of state of Fe₃S and implications for sulfur in Earth's core. Journal of Geophysical
444 Research: Solid Earth, 111.

445 Shannon, M.C. and Agee, C.B. (1996) High pressure constraints on percolative core formation.
446 Geophysical Research Letters, 23, 2717–2720.

447 Sheldrick, G.M. (2015b) Crystal structure refinement with SHELXL. Acta Crystallographica
448 Section C: Structural Chemistry, 71, 3–8.

449 Stevenson, D.J. (1981). Models of the Earth's core. Science, 214, 611–619.

450 Stevenson, D.J. (1988) Fluid dynamics of core formation. In Topical Conference Origin of the
451 Earth (Vol. 681, p. 87).

452 Tateno, S., Ozawa, H., Hirose, K., Suzuki, T., I-Kawaguchi, S., and Hirao, N. (2019) Fe₂S: the
453 most Fe-rich iron sulfide at the Earth's inner core pressures. Geophysical Research
454 Letters, 46, 11,944–11,949.

455 Thompson, S., Komabayashi, T., Breton, H., Suehiro, S., Glazyrin, K., Pakhomova, A. and
456 Ohishi, Y. (2020) Compression experiments to 126 GPa and 2500 K and thermal
457 equation of state of Fe₃S: Implications for sulphur in the Earth's core. Earth and Planetary
458 Science Letters, 534, 116080.

459 Wasson, J.T. and Wai, C.M. (1970) Composition of the metal, schreibersite and perryite of
460 enstatite achondrites and the origin of enstatite chondrites and achondrites. Geochimica et
461 Cosmochimica Acta, 34, 169-184.

462 Yoshino, T., Walter, M.J. and Katsura, T. (2003) Core formation in planetesimals triggered by
463 permeable flow. Nature, 422, 154–157.

464 Yokoo, S., Hirose, K., Sinmyo, R. and Tagawa, S. (2019) Melting experiments on liquidus phase
465 relations in the Fe-S-O ternary system under core pressures. Geophysical research letters,
466 46, 5137–5145.

467 Zurkowski, C.C., Lavina, B., Chariton, S., Tkachev, S., Prakapenka V.B. and Campbell A.J.,
468 *in press*. The crystal structure of Fe₂S at 90 GPa based on single-crystal X-ray diffraction
469 techniques. American Mineralogist, <https://doi.org/10.2138/am-2022-7973>

470 Zurkowski, C. C., Lavina, B., Brauser, N. M., Davis, A. H., Chariton, S., Tkachev, S.,
471 Greenberg, E., Prakapenka, V. B., and Campbell, A. J., *in press*. Pressure-induced C23-
472 C37 transition and compression behavior of orthorhombic Fe₂S to Earth's core pressures
473 and high temperatures. <https://doi.org/10.2138/am-2022-8187>

474

475

476 **Fe₅S₂ identified as a host for sulfur in Earth's core**

477 **Claire C. Zurkowski^a †, Barbara Lavina^{b,c}, Abigail Case^a, Kellie Swadba^a, Stella Chariton^b,**
478 **Vitali B. Prakapenka^b, Andrew J. Campbell^a**

479
480 ^aThe University of Chicago, Department of the Geophysical Sciences, 5734 S Ellis Ave, Chicago, IL 60637, USA

481 ^bCenter for Advanced Radiation Sources, The University of Chicago, 9700 South Cass Avenue, Lemont, IL 60439,
482 USA

483 ^cX-ray Science Division, Advanced Photon Source, Argonne National Laboratory, Lemont, IL 60439, USA

484 [†]Now at Earth and Planets Laboratory, Carnegie Institution for Science, 5251 Broad Branch Road, NW,
485 Washington, DC 20015, USA

486

487

488

Corresponding Author: Claire Zurkowski, czurkowski@carnegiescience.edu

489 **Supplementary Information**

490 The Supplementary Information includes:

- 491 ➤ Supplementary Information Text
- 492 ➤ Table S1
- 493 ➤ Table S2
- 494 ➤ Table S3
- 495 ➤ Table S4
- 496 ➤ Figure S1
- 497 ➤ Figure S2
- 498 ➤ Figure S3
- 499 ➤ Figure S4
- 500 ➤ Supplementary Information References

501

502

503

504

505

506

507

508

509

510 **Supplementary Information Text**

511 *Synthesis of Fe₅S₂ to 200 GPa*

512 Fe₅S₂ was synthesized between 119(2) and 193(4) GPa with heating to temperatures
513 between 2400–3300 K. The formation of Fe₅S₂ phase was first recognized in the diffraction
514 patterns by the onset of diffuse streaks and sets of closely spaced reciprocal nodes in the powder
515 diffraction images, suggesting a complex atomic arrangement (Figure 1, S1). With sustained
516 high temperatures in the samples loaded in more hydrostatic pressure media (e.g. KCl vs. SiO₂),
517 large grain growth (3 – 6 μm) was observed and the diffuse streaks became less apparent. Further
518 experiments are required to assess the role of hydrostaticity, kinetics, pressure, and temperature
519 on the disorder of this phase.

520 Recrystallization of hcp-Fe with the Fe₅S₂ crystallites at high temperatures was observed
521 in all experiments using the Fe₈₀S₂₀ and Fe₆₇S₃₃ starting powders as evidenced by the spotty
522 (100) and (101) hcp-Fe rings in Figure 1a. Fe-recrystallization with this high-temperature Fe-
523 sulfide establishes that the probed sample locations were in a Fe-saturated phase-field (Figure
524 1a) and this phase is important to consider further in the context of Fe-rich planetary cores.

525 Upon temperature quenching, rotational single-crystal X-ray diffraction scans were
526 performed across a 37–60° omega range, depending on the DAC configuration, and grains were
527 indexed in the reciprocal space to a hexagonal unit cell compatible with an Fe₅S₂ volume (Table
528 S1, Figure 1b). Three unit-cell polytypes were observed and indexed in our experiments and are
529 listed in Table S1. All indexed grains exhibit an *a* axial length of ~ 6 Å, while 3 differing *c* axial
530 lengths are observed: ~ 11, 26, and 73 Å. Diffraction mappings show that the polytypism is
531 accompanied by diffuse scattering suggesting positional disorder as the atomic arrangement
532 along the *c* axis configures at high temperatures (Figure S1). Analogous polytypism has also

533 been observed in the transition metal binary phase Pb_5As_2 (Saini et al. 1964). Decreased diffuse
534 scattering from the Fe_5S_2 grains was observed after continued heating in the KCl pressure media,
535 and grains with $a \sim 6 \text{ \AA}$, $c \sim 11 \text{ \AA}$ were indexed, indicating that this configuration is the most
536 positionally ordered arrangement relevant to these high P - T conditions. These measured unit cell
537 parameters are compatible with 6 formula units per cell volume of Fe_5S_2 .

538 The structure of a grain Fe_5S_2 synthesized at 140(2) GPa and 3070(180) K was
539 determined based on 159 observed reflections at these extreme conditions (Table S2).
540 Assessment of the systematic absences for the structure factors reduced for Fe_5S_2 suggests a
541 $P6_3cm$ space group. Structural solution and positional and displacement parameter refinement
542 converged on the Ni_5As_2 structure type (Table S2, 3; Figure 2) (Oryshchyn et al. 2011). The
543 Ni_5As_2 structure is a slight modification of the Pb_5Sb_2 structure (El-Boragy et al. 1970) where the
544 Fe6 site (Table S3) is split about its position and given half occupancy, changing its Wyckoff site
545 from 6c to 12d (Figure 2) (Oryshchyn et al. 2011). This structural modification was initiated
546 based on the large U_{22} parameter observed on the $M6$ site ($M = \text{metal}$) in Ni_5As_2 when
547 anisotropic displacement parameters were refined using a Pb_5As_2 starting model (Figure S2). In
548 the current dataset, a comparably large U_{22} value was observed on the Fe6 site resulting in an
549 oblong displacement ellipse when refining the data against the initial Pb_5As_2 structure model.
550 The Fe6 site was positionally disordered following Oryshchyn et al. (2011), and the resultant R_1
551 value was improved by around $\sim 5\%$, rendering the Ni_5As_2 structure model more compatible with
552 the current Fe_5S_2 data (Table S2). Isotropic displacement parameters showing errors $> 3\sigma$ were
553 fixed to a value equal to approximately the average displacement parameter value for Fe or S
554 (Table S2). The isotropic displacement parameter for the disordered Fe site was also fixed at an
555 average Fe_{Uiso} value (Table S2). The number of reflections collected at these extreme pressures

556 limits the number of statistically meaningful parameters to refine, and fixing displacement
557 parameters to reasonable values precludes overinterpretation of the current dataset. The high
558 isotropic displacement parameter observed on the Fe4 site may represent some vacancies on this
559 site, but the dataset is again deficient to precisely describe the site occupancy.

560 The experimental details for the solution and refinement of Fe₅S₂ to the Ni₅As₂ solution
561 model are provided in Table S2 and the atomic coordinates of Fe₅S₂ synthesized at 140(2) GPa
562 and 3070(180) K are provided in Table S3. In accordance with previous descriptions of related
563 *M₅X₂* transitional-metal binary phases (e.g. (Kjekshus et al. 1973; Oryshchyn et al. 2011), Fe₅S₂
564 can be viewed as an arrangement of 6 Fe sites and 3 S sites with the Fe1, Fe2, Fe4, and Fe6 sites
565 are in 13-fold coordination, the Fe3 and Fe5 sites are in 12-fold coordination, and the S sites are
566 in 10-fold coordination (Figure 2c). The measured bond lengths for the Fe-coordinated polyhedra
567 are provided in Table S4. All sites are coordinated by both Fe and S sites. A CIF file for Fe₅S₂
568 is provided in Appendix A1.

569 Final R₁ values \simeq 10% attest to the less-than ideal quality of the multigrain dataset as a
570 possible result of the 1-2 megabar synthesis conditions and observed *c* axial disorder and
571 stacking complexities in Fe₅S₂ (Table S2). Previous studies of isomorphic Ni₅As₂ and related
572 Pb₅As₂ at ambient conditions have also reported similar quality of refinements despite obtaining
573 significantly more reflections in the absence of a DAC (e.g. Saini et al. 1964; El-Boragy et al.
574 1970; Kjekshus et al. 1973). Notable challenges regarding the refinement of the Fe₅S₂ structure
575 model at these extreme conditions are discussed here and compared with similar difficulties
576 reported in previous characterizations of this structure.

577 Thirteen violations of the *P6₃cm* systematic absence condition: $l = 2n$ for (*0kl*), were
578 flagged during the refinement of Fe₅S₂. The reflections associated with these systematic absence

579 violations were examined in the raw diffraction images and all show low, diffuse intensity.
580 Discrepancy over the presence or absence of weak reflections with $(0kl)$, $l=2n+1$ has been
581 reported in previous investigations of Ni_5As_2 and Pb_5As_2 (e.g. Saini et al. 1964; El-Boragy et al.
582 1970; Kjekshus et al. 1973), suggesting that these studies may have also faced difficulties with
583 space group determination. Observations of these low-intensity reflections may be a result of
584 residual disorder in the stacking arrangement along the c direction, and longer heating cycles
585 may be required for the atoms to arrange into equilibrium positions. It is likewise possible that
586 varying synthesis methods for Ni_5As_2 and Pb_5As_2 in previous ambient condition studies affected
587 the c axial atomic arrangement. Ni_5As_2 and isomorphic Ni_5P_2 also exhibits a homogeneity range
588 of $\sim 71.25 - 72.7$ atomic % As (Kjekshus et al. 1973; Litasov et al., 2019), and slight
589 modifications of this structure based on varying stacking arrangements result in structures such
590 as $\text{Ni}_{31}\text{Si}_{12}$ (Frank and Schubert 1971) and $(\text{Fe, Ni})_8(\text{Si, P})_3$ (perryite) (Okada et al. 1991).
591 Attempts to refine the current Fe-sulfide phase with the $\text{Ni}_{31}\text{Si}_{12}$ or perryite structure models did
592 not improve the refinement results. Based on the presence of disorder, polytypism, anisotropic
593 vibrational motion, and nonstoichiometry in the related M_5X_2 phases, additional nuances to the
594 Fe_5S_2 structure model may be developed in future studies; however, the identification and
595 characterization of the Fe_5S_2 crystal structure determined here to 200 GPa is novel, and the
596 observations and challenges reported in this study align with that of previous analyses of Ni_5As_2
597 and Pb_5Sb_2 that were not limited by microdiffraction in a DAC at extreme conditions.

598

599 *Other sulfides observed during heating to 200 GPa*

600 Three experiments and 7 heating cycles were performed in this study between 100 and
601 200 GPa and to 3400 K, and the X-ray diffraction patterns collected upon heating provide insight

602 into the Fe-rich Fe-S phase relations at outer core pressures and to high temperatures. In each
603 heating experiment, near melting temperatures were targeted and grains of Fe₅S₂ were identified
604 upon quenching. Additional Fe-sulfides were also observed across the thermal gradient of the
605 heated spot, providing information on the lower temperature Fe-saturated phase relations in each
606 heating cycle. Upon quenching from high-temperature synthesis at 119(2) GPa, the other grains
607 in the sample were identified and indexed to a tetragonal cell with $a = 8.094(3)$ Å, $c = 3.990(2)$
608 Å, compatible with 8 formula units of Fe₃S (Table S1). The structure was then solved and refined
609 to the Fe₃P-type structure ($I-4$, $Z = 8$) (referred to herein as $I-4$ Fe₃S) in agreement with previous
610 studies (Fei et al. 2000; Seagle et al. 2006; Morard et al. 2007; Kamada et al. 2010; Kamada et
611 al. 2012; Thompson et al. 2020). The resultant structure model for Fe₃S at these conditions is
612 shown in Figure (3a), a CIF file for Fe₃S is provided in Appendix A2, and the refinement details
613 are given in Table S2. The structure can be viewed as containing 3 tetrahedrally coordinated Fe
614 sites (Blanchard et al. 2008): one Fe-site is coordinated only by S atoms with an average bond
615 length of 2.083(9) Å, another Fe site is coordinated by 3 S atoms and 1 Fe atom with an average
616 bond length of 2.146(8) Å, and the third Fe site is coordinated by 2 S and 2 Fe atoms with an
617 average bond length of 2.137(8) Å (Figure 3). The measured interatomic distances are
618 comparable to reports on other transition metal M_3X structures (e.g. Aronsson 1955; Rundqvist
619 1979).

620 After temperature quenching from 131(2) GPa and 3050(140) K, grains of Fe₃S were not
621 observed across the heated spot. Instead, orthorhombic lattices were also identified with
622 parameters $a = 4.869(2)$ Å, $b = 3.256(2)$ Å, $c = 6.139(2)$ Å, compatible with 4 formula units of
623 Fe₂S. Structural solution and refinement indicate that the Fe₂S grains adopt the $C23$ structure
624 (Co₂P type, $Pnma$, $Z = 4$) in agreement with previous structural analyses at lower pressures

625 (Zurkowski et al. *in press*). Refinement details for the structure model are given in Table S2 and
626 a CIF file for *C23* Fe₂S is provided in Appendix A3. The structure is composed of columns of
627 FeS₄ tetrahedra and columns of FeS₅ square pyramids linked along edges in the *b* direction
628 (Figure 3b). The average Fe–S bond lengths are 2.213(8) Å and 2.011(2) Å in the square
629 pyramids and tetrahedra, respectively. These values are comparable with that observed in *C23*
630 Fe₂S at 90 GPa (Zurkowski et al. *in press*).

631 Upon compression and heating at 140(2) GPa and 3070(180) K, orthorhombic grains
632 were identified in the sample chamber with $a = 4.667(2)$ Å, $3.289(1)$ Å, $6.186(4)$ Å. This unit
633 cell is similar to the *C23* Fe₂S observed at 130 GPa, but exhibits a 4 % contraction of the *a* axial
634 length, a 1% extension of the *b* and *c* axial lengths, and a 2% volume decrease. Structural
635 solution and refinement using the measured structure factors establish that Fe₂S adopts the *C37*
636 structure (Co₂Si-type, *Pnma*, *Z*=4) at these conditions (Figure 3c). A CIF file for *C37* Fe₂S is
637 provided in Appendix A4 and the analysis details are given in Table S2. In agreement with the
638 proposed *C23*–*C37* Fe₂S phase transition around 140 GPa that is accompanied 1.6% volume
639 decrease (Zurkowski et al., *in press*), this work confirms that the *C23*–*C37* transition in Fe₂S
640 occurs between 130 and 140 GPa with a similar volume change. Inherent to the *C23*–*C37*
641 transition is coordination change from the 4-fold Fe1 coordination polyhedra in the *C23* structure
642 to the 5-fold dipyramid polyhedra in the *C37* structure (Figure 3b, c). Comparing the *C23* and
643 *C37* structure models determined at 130 and 140 GPa, respectively, a 10% contraction of the
644 interatomic distance involved in the coordination change is observed (Figure S3). The average
645 Fe–S bond lengths measured in *C37* Fe₂S are 2.196(2) Å and 2.165(3) Å in the square pyramids
646 and dipyramids, respectively. These values are comparable with *C23* Fe₂S.

647

648 *Fe-rich sulfide phase relations at core-mantle boundary pressures*

649 The presented single-crystal derived structures of Fe_5S_2 , Fe_3S , $C23 \text{Fe}_2\text{S}$ and $C37 \text{Fe}_2\text{S}$
650 were then used to inform the changes in diffraction patterns collected during heating between
651 110 and 200 GPa and to ~ 3300 K. Beginning at 112 GPa, diffraction signal from $C23 \text{Fe}_2\text{S}$
652 coexisting with Fe was first identified upon heating of the $\text{Fe}_{80}\text{S}_{20}$ starting material to ~ 2000 K.
653 With continued heating, peaks associated with tetragonal Fe_3S were observed over a limited
654 temperature range ($\lesssim 2400$ K) until diffuse scattering signal and Bragg reflections from Fe_5S_2
655 first appeared. Crystallization of the Fe_5S_2 grains with iron occurred with continued heating to
656 119(2) GPa and 2840(180) K. Upon heating beginning at 120 GPa, $C23 \text{Fe}_2\text{S}$ was observed
657 coexisting with Fe to 122(1) GPa and 2290(120) K, above which the onset of diffraction from
658 the Fe_5S_2 phase was identified and Fe_5S_2 crystallites formed coexisting with hcp-Fe to 131(2)
659 GPa and 3050(140) K. $I-4 \text{Fe}_3\text{S}$ was not observed. With continued heating cycles between 133(1)
660 GPa and 194(2) GPa and up to 3300 K, $C37 \text{Fe}_2\text{S}$ coexists with Fe at moderate temperatures and
661 a phase transition to Fe_5S_2 occurs at high temperatures. A phase diagram satisfying these
662 observations is proposed in Figure 4, and integrated XRD patterns for the heating cycles at
663 119(2) and 184(3) GPa and to 3300 K are shown in Figure S4 to demonstrate the identification
664 of $C23 \text{Fe}_2\text{S}$, Fe_3S , $C37 \text{Fe}_2\text{S}$, and Fe_5S_2 coexisting with hcp-Fe. The peak intensities from the
665 Fe_5S_2 lattices vary during heating up at high temperatures as a result of disorder, polytypism, and
666 the formation of large crystallites at high temperatures (Figure 1, S1). These structural
667 complexities render the powder diffraction patterns difficult to characterize without
668 incorporating single-crystal XRD techniques.

669

670 *Discrepancies among the current and previous studies*

671 Transitional metal binary compounds with metal-to-nonmetal ratios ranging from 2.33–
672 2.66 (~70–73 atm% metal) predominantly adopt complex trigonal or hexagonal structures with
673 considerable metal-metal bonding (Chen and Whitmire 2018 and references therein). Our
674 observations of the disorder, polytypism, and complex coordination environments inherent to
675 Fe₅S₂ demonstrate that it aligns with this systematic characterization. Interestingly, the Fe₅S₂
676 atomic arrangement is thermodynamically favored at the extreme conditions of Earth's outer
677 core over that of *I*-4 Fe₃S. These results are contrary to previous reports of Fe₃S stability on to
678 high temperatures in Fe-rich systems to 250 GPa (Kamada et al. 2010; Kamada et al. 2012;
679 Ozawa et al. 2013; Mori et al. 2017). Few lines of reasoning may account for these
680 discrepancies. Interpretation of Fe₅S₂ in the integrated powder diffraction patterns is difficult due
681 to the variation in diffraction signal obtained from the Fe₅S₂ polytypes and the low intensity
682 scattering from the disordered sites during its formation. Fe₅S₂ also forms large crystallites,
683 limiting the orientations of the phase and rendering indexation of all diffraction angles for Fe₅S₂
684 quite challenging without rotating the sample. The implementation of single-crystal X-ray
685 diffraction techniques at high pressures was critical in the current study to accurately
686 characterize the hexagonal unit cell geometry and complex structure of the Ni₅As₂-like Fe₅S₂.

687 Several studies have also reported chemically analyzed Fe₃S grains in samples recovered
688 from high temperatures in the 200–250 GPa range (Mori et al. 2017; Yokoo et al. 2019; Ozawa
689 et al. 2013), but the difference in Fe content between Fe₃S and Fe₅S₂ may be as few as 3%. This
690 value is generally within 3 sigma of the atomic percent error reported for chemical analyses of
691 samples recovered from these extreme conditions, posing another challenge for distinguishing
692 between the synthesis of Fe₃S and Fe₅S₂. Furthermore, based on characterizations of the

693 isomorphous Ni_5As_2 and Ni_5P_2 , these structures exhibit a homogeneity range with up to ~73 atm%
694 metal (Kjekshus et al. 1973; Litasov et al., 2019). For example, TEM analysis of a Fe–S sample
695 recovered from 236 GPa and 2980 K reveals sulfide grains with on average ~73 atm% Fe
696 (Ozawa et al. 2013). This value is within 0.3–1.25 atomic percent of the possible range of Fe_5S_2
697 stoichiometries and 2 atomic percent less than an Fe_3S composition. The results from this
698 previous work as well as other chemical analyses of samples recovered from outer core pressures
699 and high temperatures therefore do not contradict the current results (Mori et al. 2017; Yokoo et
700 al. 2019; Ozawa et al. 2013) and may reveal a previous misinterpretation of Fe_5S_2 as Fe_3S based
701 on measured chemistries.

702

703

704 **Table S1.** Unit cell parameters of Fe₅S₂, Fe₃S, and Fe₂S measured upon quenching from high *P*-
705 *T* synthesis in this study. Each cell was indexed in the reciprocal space, and the DAC opening,
706 and number of reflections obtained for each lattice are listed. For select experiments, high-
707 temperature synthesis was conducted without collecting X-ray diffraction data, and the synthesis
708 conditions for these experiments are listed as “high T, not measured.”

Sample name	Starting		Phase	Room temperature collection							Synthesis conditions	
	material	medium		P	<i>a</i>	<i>b</i>	<i>c</i>	V	DAC opening	no. of reflections	<i>P</i>	<i>T</i>
				GPa	Å	Å	Å	Å ³	(°)		GPa	K
C140_P2_map25	Fe80S20	KCl	Fe5S2	105(2)	6.020(4)		11.204(7)	351.6(5)	60	290	119(2)	2840(140)
C140_P2_map31	Fe80S20	KCl	Fe5S2	105(2)	6.050(2)		73.0(2)	2313(1)	60	134	119(2)	2840(140)
C140_P4_map10	Fe80S20	KCl	Fe5S2	118(1)	5.983(3)		11.078(6)	343.4(4)	60	489	140(2)	3070(180)
C140_P4_map14	Fe80S20	KCl	Fe5S2	118(1)	5.979(2)		11.084(4)	343.2(3)	60	379	140(2)	3070(180)
C140_P4_map14	Fe80S20	KCl	Fe5S2	118(1)	5.973(1)		11.094(2)	342.8(1)	60	276	140(2)	3070(180)
C129_P140_map71	Fe67S33	SiO2	Fe5S2	136.4(5)	5.957(4)		71.89(4)	2209(3)	34	84	159(2)	3230(150)
C129_P150_map9	Fe67S33	SiO2	Fe5S2	144.2(8)	5.939(3)		25.99(6)	794(2)	34	76	high T, not measured	
C129_P150_map9	Fe67S33	SiO2	Fe5S2	144.2(8)	5.923(1)		26.004(6)	789.9(3)	34	146	high T, not measured	
C137_P1_map25	Fe80S20	SiO2	Fe5S2	159(1)	5.890(3)		25.837(7)	776.2(5)	40	108	184(3)	3250(260)
C137_P1_map25	Fe80S20	SiO2	Fe5S2	159(1)	5.880(1)		25.789(3)	772.0(2)	40	108	184(3)	3250(260)
C137_P1_map25	Fe80S20	SiO2	Fe5S2	159(1)	5.876(2)		25.884(8)	774.0(4)	40	116	184(3)	3250(260)
C137_P1_map25	Fe80S20	SiO2	Fe5S2	159(1)	5.883(3)		25.85(1)	774.6(7)	40	126	184(3)	3250(260)
C137_P1	Fe80S20	SiO2	Fe5S2	159(1)	5.897(3)		25.90(1)	775.1(6)	40	116	184(3)	3250(260)
C137_P1	Fe80S20	SiO2	Fe5S2	159(1)	5.878(1)		25.784(3)	771.6(2)	40	149	184(3)	3250(260)
C137_P2_34	Fe80S20	SiO2	Fe5S2	179(1)	5.8400(7)		25.583(2)	755.7(1)	40	189	193(4)	3010(160)
C140_P1_map	Fe80S20	KCl	Fe3S	100(1)	8.156(3)		4.025(3)	267.8(3)	60	416	high T, not measured	
C140_P2_map25	Fe80S20	KCl	Fe3S	105(2)	8.094(3)		3.990(2)	261.4(2)	60	296	119(2)	2840(140)
C140_P3_map6	Fe80S20	KCl	C23Fe2S	111(1)	4.869(2)	3.256(2)	6.139(2)	97.3(1)	60	227	131(2)	3050(140)
C140_P4_map10	Fe80S20	KCl	C37Fe2S	118(1)	4.677(2)	3.289(1)	6.186(4)	95.18(9)	60	188	140(2)	3070(180)

709
710
711
712
713
714
715
716
717
718
719
720
721
722
723
724
725

726 **Table S2.** Select experimental details for crystal structure synthesis and analysis of Fe₅S₂, Fe₃S,
 727 and the Fe₂S polymorphs.

Phase	Fe ₅ S ₂	Fe ₃ S	C23 Fe ₂ S	C37 Fe ₂ S
Sample Name	C140_P4_map10	C140_P2_map25	C140_P3_map6	C140_P4_map10
Synthesis				
Pressure (GPa)	140(2)	119(2)	131(2)	140(2)
Synthesis Temperature (K)	3070(180)	2840(140)	2050(140)	3070(180)
Symmetry	Hexagonal, <i>P6(3)cm</i> , Z=6	Tetragonal, <i>I-4</i> , Z=8	Orthorhombic, <i>Pnma</i> , Z = 4	Orthorhombic, <i>Pnma</i> , Z = 4
<i>a</i> (Å)	5.979(2)	8.094(3)	4.869(3)	4.677(2)
<i>b</i> (Å)			3.256(4)	3.289(1)
<i>c</i> (Å)	11.087(6)	3.990(2)	6.139(2)	6.186(4)
<i>V</i> (Å ³)	343.2(3)	226.4(2)	97.3(1)	95.18(9)
Reduction				
No. of measured, independent and observed [<i>I</i> > 2σ(<i>I</i>)] reflections	396, 309, 157	332, 314, 219	227, 208, 112	188, 158, 105
<i>R</i> _{int} , <i>R</i> _{sigma}	0.092, 0.062	0.053, 0.072	0.012, 0.016	0.009, 0.014
Refinement				
<i>R</i> [<i>F</i> ² > 2σ(<i>F</i> ²)], <i>wR</i> (<i>F</i> ²), <i>S</i>	0.098, 0.255, 1.12	0.067, 0.164, 1.05	0.053, 0.149, 1.21	0.047, 0.139, 1.22
No. of reflections	156	219	112	105
No. of parameters	21	17	10	10
Δρ _{max} , Δρ _{min} (e Å ⁻³)	2.14, -2.18	1.92, -1.68	1.86, -2.02	1.91, -2.21

728
 729
 730
 731
 732
 733

734 **Table S3.** Atomic coordinates of the Fe₅S₂ refinement model for the data collected at 140(2) GPa
 735 and quenched from 3070(180) K.

Wycoff site	ATOM	x	y	z	Uiso
2a	Fe1	0	0	0.963	0.021
	error			0.003	0.005
4b	Fe2	1/3	2/3	0.089	0.046
	error			0.003	0.005
6c	Fe3	0.259	0	0.126	0.021
	error	0.002		0.001	
6c	Fe4	0.613	0	0.222	0.021
	error	0.002		0.001	0.003
6c	Fe5	0.284	0	0.330	0.027
	error	0.002		0.001	0.003
12d	Fe6*	0.651	0.056	0.426	0.021
	error	0.003	0.003	0.002	
2a	S1	0	0	0.220	0.026
	error			0.004	
4b	S2	1/3	2/3	0.299	0.026
	error			0.002	
6c	S3	0.673	0	0.030	0.026
	error	0.005		0.003	

*indicates half occupancy

736
 737
 738
 739
 740
 741
 742
 743
 744
 745
 746
 747
 748

749 **Table S4.** Selected interatomic distances for the Fe sites measured in Fe₅S₂ at 140 GPa.

Atom	bonded to	#	distance (Å)
Fe1	-Fe3	3	2.39(2)
	-Fe5	3	2.22(3)
	-Fe6	3	2.313(17)
	-S1	1	2.66(8)
	-S4	3	2.09(3)
Fe2	-Fe3	3	2.275(3)
	-Fe4	3	2.375(16)
	-Fe6	3	2.40(3)
	-S3	1	2.36(4)
	-S4	3	2.108(13)
Fe3	-Fe1	1	2.39(2)
	-Fe2	2	2.275(8)
	-Fe4	3	2.350(15)
	-Fe5	1	2.30(3)
	-Fe6	1	2.307(17)
	-S1	1	1.90(4)
	-S4	3	2.68(3)
Fe4	-Fe2	2	2.375(16)
	-Fe3	3	2.320(11)
	-Fe5	3	2.416(14)
	-Fe6	1	2.303(17)
	-S1	1	2.326(11)
	-S3	2	2.044(16)
	-S4	1	2.10(3)
Fe5	-Fe1	1	2.22(3)
	-Fe3	1	2.30(3)
	-Fe4	3	2.416(14)
	-Fe6	3	2.135(15)
	-S1	1	2.09(5)
	-S3	2	2.184(10)
	-S4	1	2.27(3)
Fe6	-Fe1	1	2.313(17)
	-Fe2	2	2.40(3)
	-Fe3	1	2.307(17)
	-Fe4	1	2.303(17)
	-Fe5	3	2.135(15)
	-S3	2	2.15(3)
	-S4	3	2.17(3)

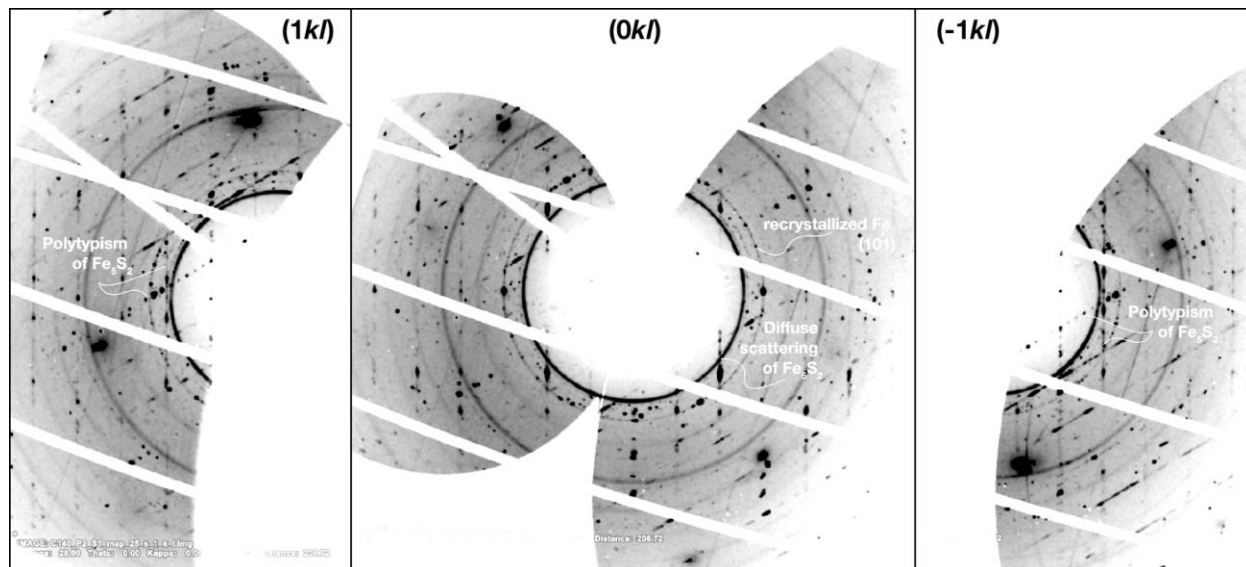
750

751

752

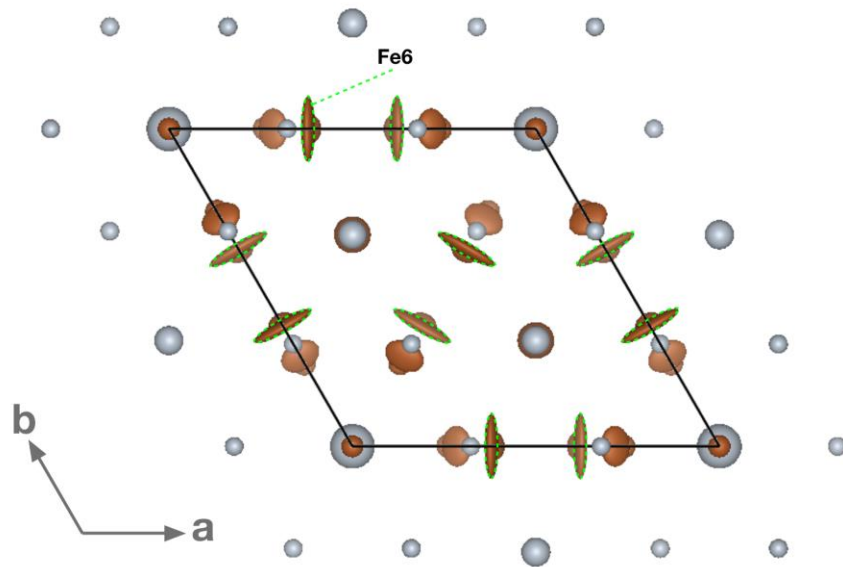
753

754 **Figure S1.** Unwarped diffraction mappings of the $(1kl)$, $(0kl)$, and $(-1kl)$ directions for an Fe_5S_2
755 crystallite exemplifying the diffuse scattering signal collected at 119(2) and 2840(180) K. The
756 $(1kl)$ and $(-1kl)$ mappings also show the presence of a polytype with more closely spaced
757 reflections oriented $\sim 51^\circ$ from the mapped crystallite.



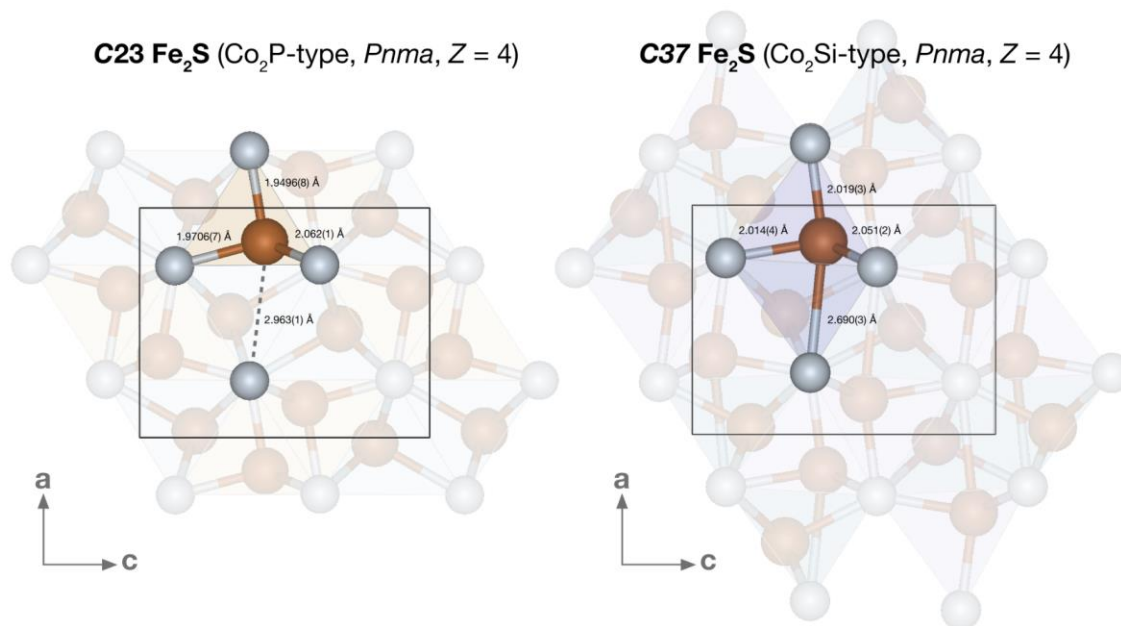
758
759
760
761
762
763
764

765 **Figure S2.** Fe_5As_2 structure model shown with anisotropic displacement ellipsoids using the
766 starting Pb_5As_2 structure model. In accordance with the Ni_5As_2 structural characterization
767 (Oryshchyn et al. 2011), these sites were disordered about their position and ascribed half
768 occupancy.

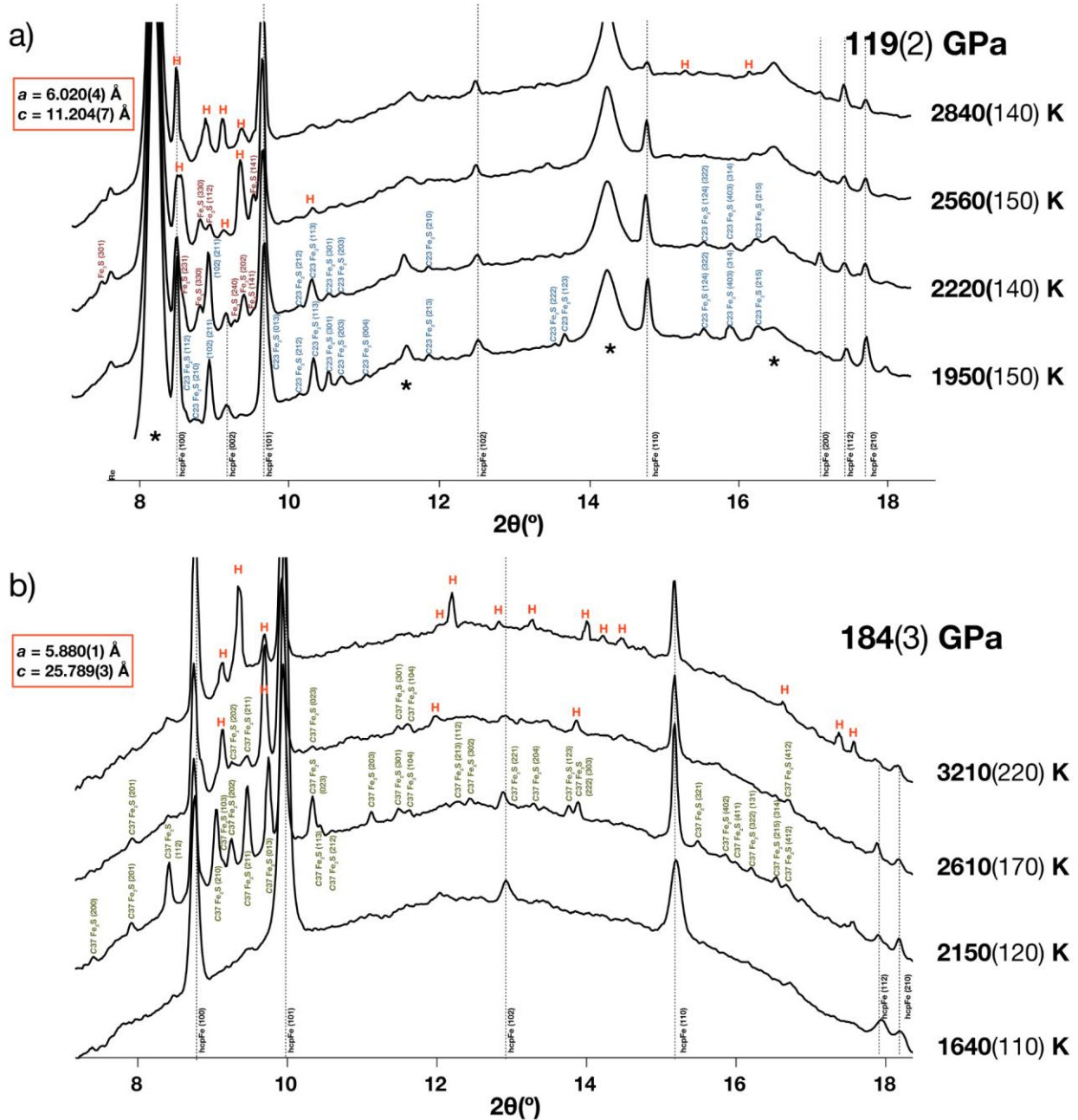


769
770
771
772
773
774
775
776
777
778
779
780
781
782
783
784
785
786
787

788 **Figure S3.** Comparison of the *C23* and *C37* structure models refined at 130 and 140 GPa,
789 respectively. In the *C23* Fe₂S structure, the next nearest sulfur site to the Fe1 tetrahedral site is at
790 a 2.963(1) Å distance at 130 GPa (dotted line). A 10% contraction of this interatomic distance
791 and a coordination change is observed in the formation of *C37* Fe₂S at 140 GPa (right).
792



812 **Figure S4.** X-ray diffraction patterns collected upon heating in an Fe₈₀S₂₀ starting composition at
 813 a) 119(2) GPa and b) 184(3) GPa. The miller indices for C23 Fe₂S (blue), Fe₃S (burgundy), and
 814 C37 Fe₂S (green) are provided, and the red “H” symbols represent the observations of the
 815 formation of Fe₅S₂. The growth of large crystallites, along with the disorder and polytypism of
 816 this phase make for challenging powder diffraction indexing, but the lattice parameters of Fe₅S₂
 817 indexed in the reciprocal space after quenching from these high *P-T* conditions are provided.



818
 819

820

821 **Supplementary Information References**

- 822 Aronsson, B. (1955) The crystal structure of Ni₃P. (Fe₃P-Type). *Acta Chemica Scandinavica*, 9,
823 137-140.
- 824 Blanchard, P.E., Grosvenor, A.P., Cavell, R.G. and Mar, A. (2008) X-ray Photoelectron and
825 Absorption Spectroscopy of Metal-Rich Phosphides M₂P and M₃P (M=
826 Cr– Ni). *Chemistry of Materials*, 20, 7081-7088.
- 827 Chen, J.H. and Whitmire, K.H. (2018) A structural survey of the binary transition metal
828 phosphides and arsenides of the d-block elements. *Coordination Chemistry Reviews*, 355,
829 271–327.
- 830 El-Boragy, M., Bhan, S. and Schubert, K. (1970) Kristallstruktur von Pd₅Sb₂ und Ni₅As₂ und
831 einigen varianten. *Journal of the Less Common Metals*, 22, 445–458.
- 832 Fei, Y., Li, J., Bertka, C.M. and Prewitt, C.T. (2000) Structure type and bulk modulus of Fe₃S, a
833 new iron-sulfur compound. *American Mineralogist*, 85, 1830–1833.
- 834 Frank, K. and Schubert, K. (1971) Kristallstruktur von Ni₃₁Si₁₂. *Acta Crystallographica Section*
835 *B: Structural Crystallography and Crystal Chemistry*, 27, 916–920.
- 836 Kamada, S., Terasaki, H., Ohtani, E., Sakai, T., Kikegawa, T., Ohishi, Y., Hirao, N., Sata, N. and
837 Kondo, T. (2010) Phase relationships of the Fe–FeS system in conditions up to the
838 Earth's outer core. *Earth and Planetary Science Letters*, 294, 94–100.
- 839 Kamada, S., Ohtani, E., Terasaki, H., Sakai, T., Miyahara, M., Ohishi, Y. and Hirao, N. (2012)
840 Melting relationships in the Fe–Fe₃S system up to the outer core conditions. *Earth and*
841 *Planetary Science Letters*, 359, 26–33.
- 842 Kjekshus, A., Skaug, K.E., Hebrew, C., Van Buren, C.T., Klæboe, P. and Swahn, C.G. (1973).
843 On the crystal structure of Ni₅As₂. *Acta Chem. Scand.*, 27, 582–588.
- 844 Litasov, K.D., Shatskiy, A.F., Minin, D.A., Kuper, K.E. and Ohfuji, H. (2019). The Ni–Ni₂P
845 phase diagram at 6 GPa with implication to meteorites and super-reduced terrestrial
846 rocks. *High Pressure Research*, 39, 561–578.
- 847 Morard, G., Andrault, D., Guignot, N., Sanloup, C., Mezouar, M., Petitgirard, S. and Fiquet, G.
848 (2008). In situ determination of Fe–Fe₃S phase diagram and liquid structural properties
849 up to 65 GPa. *Earth and Planetary Science Letters*, 620–626.
- 850 Mori, Y., Ozawa, H., Hirose, K., Sinmyo, R., Tateno, S., Morard, G. and Ohishi, Y. (2017)
851 Melting experiments on Fe–Fe₃S system to 254 GPa. *Earth and Planetary Science Letters*,
852 464 135–141.
- 853 Okada, A., Kobayashi, K., Ito, T. and Sakurai, T. (1991) Structure of synthetic perryite,
854 (Ni, Fe)₈(Si, P)₃. *Acta Crystallographica Section C: Crystal Structure Communications*,
855 47, 1358–1361.
- 856 Oryshchyn, S., Babizhetskyy, V., Zhak, O., Stoyko, S., Guérin, R., and Simon, A. (2011) Crystal
857 structure of HT-Ni₅P₂ and reinvestigation of isotypic Ni₅As₂. *Intermetallics*, 19,
858 1041–1046.
- 859 Ozawa, H., Hirose, K., Suzuki, T., Ohishi, Y. and Hirao, N. (2013) Decomposition of Fe₃S
860 above 250 GPa. *Geophysical research letters*, 40, 4845–4849.

861 Rundqvist, S. (1960) The structures of Co_2P , Ru_2P and related phases. *Acta Chemica*
862 *Scandinavica*, 14, 1961–1979.

863 Rundqvist, S. and Jellinek, F. (1959) The structures of $\text{Ni}_6\text{Si}_2\text{B}$, Fe_2P and some related phases.
864 *Acta Chemica Scandinavica*, 13, 425–432.

865 Saini, G.S., Calvert, L.D., and Taylor, J.B. (1964). Compounds of the type M_5X_2 : Pd_5As_2 , Ni_5Si_2 ,
866 and Ni_5P_2 . *Canadian Journal of Chemistry*, 42, 1511–1517.

867 Seagle, C.T., Campbell, A.J., Heinz, D.L., Shen, G. and Prakapenka, V.B. (2006) Thermal
868 equation of state of Fe_3S and implications for sulfur in Earth's core. *Journal of Geophysical*
869 *Research: Solid Earth*, 111.

870 Thompson, S., Komabayashi, T., Breton, H., Suehiro, S., Glazyrin, K., Pakhomova, A. and
871 Ohishi, Y. (2020) Compression experiments to 126 GPa and 2500 K and thermal
872 equation of state of Fe_3S : Implications for sulphur in the Earth's core. *Earth and Planetary*
873 *Science Letters*, 534, 116080.

874 Yokoo, S., Hirose, K., Sinmyo, R. and Tagawa, S. (2019) Melting experiments on liquidus phase
875 relations in the Fe-S-O ternary system under core pressures. *Geophysical research letters*,
876 46, 5137–5145.

877 Zurkowski, C.C., Lavina, B., Chariton, S., Tkachev, S., Prakapenka V.B. and Campbell A.J.,
878 *in press*. The crystal structure of Fe_2S at 90 GPa based on single-crystal X-ray diffraction
879 techniques. *American Mineralogist*, <https://doi.org/10.2138/am-2022-7973>

880 Zurkowski, C. C., Lavina, B., Brauser, N. M., Davis, A. H., Chariton, S., Tkachev, S.,
881 Greenberg, E., Prakapenka, V. B., and Campbell, A. J., *in press*. Pressure-induced C23-
882 C37 transition and compression behavior of orthorhombic Fe_2S to Earth's core pressures
883 and high temperatures. <https://doi.org/10.2138/am-2022-8187>
884
885